International Journal of Thermal Sciences 176 (2022) 107493

Contents lists available at ScienceDirect

International Journal of Thermal Sciences

journal homepage: www.elsevier.com/locate/ijts

Substrate effects on the near-field radiative heat transfer between bi-planar graphene/hBN heterostructures

Bei Yang [a], Deng Pan [c], Xiangdong Guo [a], Hai Hu [a], Qing Dai [a,b,*]

[a] CAS Key Laboratory of Nanophotonic Materials and Devices, CAS Key Laboratory of Standardization and Measurement for Nanotechnology, CAS Center for Excellence in Nanoscience, National Center for Nanoscience and Technology, Beijing, 100190, China
[b] Center of Materials Science and Optoelectronics Engineering, University of Chinese Academy of Sciences, Beijing, 100049, China
[c] State Key Laboratory of Precision Spectroscopy, East China Normal University, Shanghai, China

ARTICLE INFO

Keywords:
Near-field radiative heat transfer
Surface polaritons
Graphene/hBN heterostructure
Substrate effect

ABSTRACT

The hybridization of surface plasmon polaritons and hyperbolic phonon polaritons in graphene/hBN heterostructures has been well documented to achieve very high radiative heat flux transferred in the near field, paving the way for wide applications ranging from energy harvesting, non-contact thermal management to thermal imaging. However, previous related theoretical studies mainly focused on suspended structures. When it comes to the experimental implementation, a supporting substrate is quite a necessity for this kind of 2D layered heterostructures to ensure structural stability. Herein, the near-field radiative heat transfer (NFRHT) between bi-planar graphene/hBN heterostructures was revisited by integrating them with various substrates, including Au, SiC, and silica, under the framework of the fluctuation-dissipation theorem. The results show that each substrate exerts significant impacts either further enhancing or suppressing the NFRHT between those bi-planar heterostructures, due to the competition between polaritonic couplings and dielectric losses. Whereas, these substrate effects depend on the hBN thickness with a critical length, beyond which the hBN itself is thick enough to indiscriminately screen all these effects. The findings in this study will be instructive to both the experimental designs and device integrations for graphene-based NFRHT applications.

1. Introduction

Recent years have seen an increasing interest in studying near-field radiative heat transfer (NFRHT) because of its great potential in various applications, such as energy harvesting [1,2], non-contact thermal management [3,4], thermal imaging [5,6], heat-assisted magnetic recording [7], and nanolithography [8], etc. As a typical model system for the NFRHT, when two planar surfaces at different temperatures are separated by a vacuum gap with a spacing shorter than the characteristic thermal peak wavelength ($d < \lambda_{Th} = \hbar c / k_B T$, about 9.6 μm at room temperature), i.e. in the near-field regime, the radiative heat transfer between them can exceed the blackbody limit by several orders of magnitude [9]. This astonishing enhancement stems from the contribution of evanescent waves, which open paths for photon tunneling that allows additional thermal energy to transfer through [10]. The NFRHT can be further enhanced when materials supporting surface polaritons in the infrared ranges are involved, making it more appealing to applications associated with high heat flux, such as micro/nanoscale electronic cooling [3,11].

Tremendous efforts have been devoted to enhancing NFRHT via exploring innovative materials, structure configurations as well as surface engineering both experimentally and numerically [12,13]. The metallic and polar dielectric materials have been demonstrated to enhance the NFRHT due to the induced eddy currents, the excitations of surface plasmon polaritons (SPPs), and surface phonon polaritons (SPhPs) [14–19]. Besides, anisotropic metamaterials including nanowires [20], carbon nanotubes [21], multilayers [22,23], gratings [24], and others [25] have also been reported to significantly enhance the NFRHT due to the hyperbolic modes enabling larger transverse wavevectors. Among those, 2D van der Waals (vdW) materials represented by graphene [26] and black phosphorus (BP) [27] have been demonstrated to strongly mediate, enhance and tailor NFRHT due to their merits including the single-atom-layer thickness, wideband frequency response within infrared ranges, as well as rich and highly tunable polaritonic

* Corresponding author. CAS Key Laboratory of Nanophotonic Materials and Devices, CAS Key Laboratory of Standardization and Measurement for Nanotechnology, CAS Center for Excellence in Nanoscience, National Center for Nanoscience and Technology, Beijing, 100190, China.
E-mail address: daiq@nanoctr.cn (Q. Dai).

https://doi.org/10.1016/j.ijthermalsci.2022.107493
Received 8 November 2021; Received in revised form 20 January 2022; Accepted 23 January 2022
Available online 3 February 2022
1290-0729/

modes. Vertical multilayered heterostructures via restacking exfoliated and/or epitaxial vdW layers provide an ideal material platform to deliver new optical responses beyond those of the individual constituents through effective coupling between various polaritonic modes, thus enabling to further enhance and tailor the NFRHT. For instance, the in-plane anisotropy of layered BP together with its highly tunable SPPs has been exploited to modulate the NFRHT by the mechanical rotation [27,28]. Besides, the hybridization of SPPs and hyperbolic phonon polaritons (HPPs) in graphene/hBN heterostructures yielded new polaritonic modes featuring as much stronger field confinement and lower energy losses [29]. When these heterostructures are symmetrically arranged into a bi-planar configuration separated by a vacuum nanogap, the hybridized modes can promote the photon tunneling and enhance the NFRHT far beyond the blackbody limit by 4 orders of magnitude [30]. This has been numerically investigated in some literature in terms of both single-layered and multilayered configurations [30–32]. However, these studies were all based on suspended structures with very thin hBN layers, ignoring the possible effects of substrates. When considering experimental implementations, a supporting substrate is quite a necessity for these 2D layered heterostructures to ensure structural stability. In fact, both SPPs and SPhPs are strongly sensitive to the dielectric environments or supporting substrates, due to the interactions with surrounding phonons, accumulated charges, and impurities, etc. [33], which greatly impact their properties and thus the NFRHT between.

Therefore, in this study, we theoretically reexamined the NFRHT between graphene/hBN heterostructures by respectively integrating them with various substrates including Au, SiC, and silica. The role that these substrates play in terms of enhancing or suppressing NFRHT was particularly addressed, together with the underlying mechanisms.

2. Model system

Fig. 1a) schematically illustrates the NFRHT between two parallel planar heterostructures separated by a vacuum gap with a distance of d. Each heterostructure consists of a top graphene monolayer, a thin hBN spacer layer with a thickness h_{hBN}, and a bottom substrate with a thickness of 2 μm. These heterostructures are at thermal equilibrium but under different temperatures. The emitter is at a relatively higher temperature of T_h while the receiver is at a lower one of T_c. In this study, T_h is set to be 323 K while T_c keeps at room temperature of 300 K. Note that the surface polaritons will be thermally excited on the whole surfaces of both heterostructures, and Fig. 1a) is only for schematic demonstration.

2.1. Material properties

Previous studies on NHRHT between graphene-based heterostructures modeled graphene as a surface current through its 2D conductivity that exerts on the beneath media [30,32]. Equivalently, the graphene can also be treated as a finite layer with a thickness of h_g and characterized by an effective dielectric function [34]

$$\varepsilon(\omega,h)=1+\frac{i\sigma(\omega)}{\varepsilon_0\omega h_g}, \tag{1}$$

where ε_0 is the vacuum permittivity, ω is the angular frequency, and σ is the in-plane optical conductivity of graphene. The surface conductivity can be fully captured by the Kubo formula [35], which at the room temperature T, i.e., $k_BT \ll E_{\mathrm{F}}$, can be adequately approximated as [36]

$$\sigma=\frac{ie^2E_{\mathrm{F}}}{\pi\hbar^2(\omega+i\tau^{-1})}+i\frac{e^2}{4\pi\hbar}\ln\left[\frac{2|E_{\mathrm{F}}|-\hbar(\omega+i\tau^{-1})}{2|E_{\mathrm{F}}|+\hbar(\omega+i\tau^{-1})}\right], \tag{2}$$

where the two terms on the right denote the contributions of intra- and inter-band transitions, respectively. Besides, $\tau=\mu_{\mathrm{cm}}E_{\mathrm{F}}/ev_{\mathrm{F}}^2$ is the relaxation time, μ_{cm} is the carrier mobility, E_{F} is the doped graphene Fermi energy or chemical potential, and v_{F} is the Fermi velocity. In this study, parameters for graphene monolayer [37] were adopted as $h_g = 0.334\ nm$, $\mu_{cm} \approx 2000\ \mathrm{cm^2/(V\cdot s)}$, $E_{\mathrm{F}} = 0.3$ eV, $v_{\mathrm{F}} = c/300 = 10^6$ m/s, unless otherwise specified.

Hexagonal boron nitride (hBN) is a natural hyperbolic material that supports HPPs within the reststrahlen bands (RBs), which are defined by the material itself and locate within phonon frequencies of transverse-optical (TO) and longitudinal-optical (LO). The RBs are characterized by a negative real part of the dielectric constant, based on which two types of HPPs can be excited in the hBN layer (Type I: $\varepsilon_\perp > 0, \varepsilon_\parallel < 0$; and Type II: $\varepsilon_\perp < 0,\ \varepsilon_\parallel > 0$). The infrared optical response of hBN has been extensively investigated via both experimental measurements and first-principle calculations [38,39]. A consensus has been reached that both the in-plane and out-of-plane dielectric function can each be approximated by the well-known Lorentz model as

$$\varepsilon_{\mathrm{hBN,m}}=\varepsilon_{\infty,\mathrm{m}}\left[1+\frac{(\omega_{\mathrm{LO},m})^2-(\omega_{\mathrm{TO},m})^2}{(\omega_{\mathrm{TO},m})^2-\omega^2-i\omega\Gamma_m}\right], \tag{3}$$

where subscript $m = \perp$ or $\parallel$, denotes the in-plane and out-of-plane component corresponding to the direction perpendicular or parallel to the optical axis, respectively; $\varepsilon_{\infty,\mathrm{m}}$ is the high-frequency permittivity; $\omega_{\mathrm{LO,m}}$ and $\omega_{\mathrm{TO,m}}$ are the LO and TO phonon frequencies, respectively; and Γ_m is the damping constant. Here the fitting parameters are given as [38,39]: $\varepsilon_{\parallel,\infty} = 2.8$, $\omega_{\mathrm{LO},\parallel} = 845\ \mathrm{cm^{-1}}$, $\omega_{\mathrm{TO},\parallel} = 785\ \mathrm{cm^{-1}}$, $\Gamma_\parallel = 1\ \mathrm{cm^{-1}}$; while $\varepsilon_{\perp,\infty} = 3$, $\omega_{\mathrm{LO},\perp} = 1630\ \mathrm{cm^{-1}}$, $\omega_{\mathrm{TO},\perp} = 1395\ \mathrm{cm^{-1}}$, $\Gamma_\perp = 2\ \mathrm{cm^{-1}}$. As displayed in Fig.S1 a) in the supplementary information (SI), the shaded regions indicate that HPPs can be excited in two RBs. It

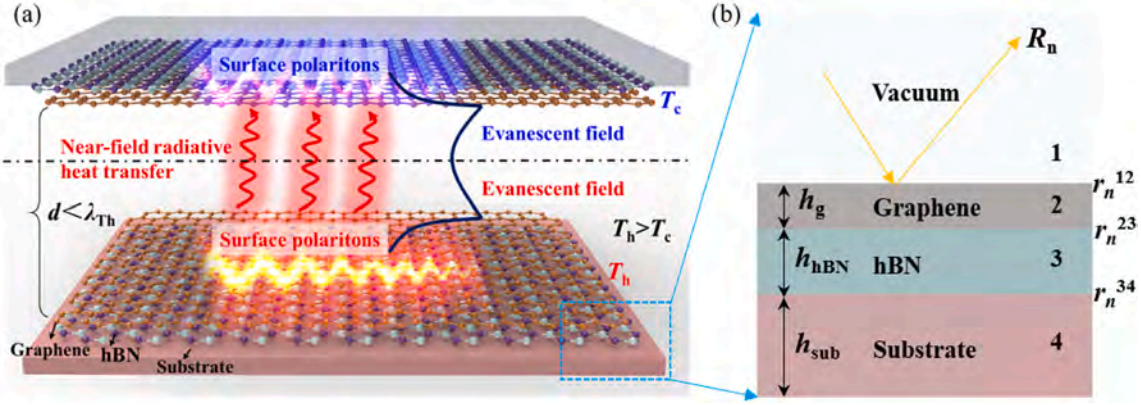

Fig. 1. a) Schematic diagram of NFRHT between bi-planar graphene/hBN/substrate heterostructures separated by a vacuum gap; b) Insets for detailed layers of one planar heterostructure.

should be noted that for very thin layers, the inherent dielectric loss of hBN becomes larger where the phonon damping constant Γ should take larger values [40]. This effect was not considered in the present study. The dielectric functions for Au, SiC, and silica can be found in Ref. [41].

2.2. NFRHT calculation based on fluctuation-dissipation theorem

In this study, we focus on the NFRHT between bi-planar structures, which are constructed by two identical units and separated by a vacuum gap, just as the system of our main interest shown in Fig. 1a) with detailed layer configurations in insets of Fig. 1b). Based on the fluctuation-dissipation theorem (FDT), the radiative heat flux q can be calculated as [42].

$$q=\frac{1}{4\pi^2}\int_0^\infty [\Theta(\omega,T_1)-\Theta(\omega,T_2)]d\omega\int_0^\infty \left[\xi_s(\omega,\beta)+\xi_p(\omega,\beta)\right]\beta d\beta, \tag{4}$$

where the two structure units are assumed to be equilibrated at temperatures T_1 and T_2; $\Theta(\omega,T)=\hbar\omega/[\exp(\hbar\omega/k_BT)-1]$ is the average energy of a Planck oscillator; β is the magnitude of the in-plane transverse wave vector; subscripts s and p denote s- or p-polarized modes, i.e., the transverse electric (TE) and transverse magnetic (TM) waves, respectively; and $\xi(\omega,\beta)$ is the energy transmission coefficient.

As indicated by the second integral in Eq. (4),the total heat flux q receives contributions of both the far-field ($\beta\le k_0$, propagating modes) and near-field ($\beta>k_0$, evanescent modes). In the near field $\beta>k_0$, $\xi(\omega,\beta)$ is also termed photon tunneling probability (PTP). Note that the second integration in Eq. (4) over transverse wave vector, i.e., $\int_0^\infty[\xi_s(\omega,\beta)+\xi_p(\omega,\beta)]\beta d\beta$, is the spectral heat flux defining the heat flux per unit of frequency or photon energy [25].

The energy transmission coefficient $\xi_n(\omega,\beta)$ in Eq. (4) can be obtained by considering the optical reflections in such multilayer systems

$$\xi_n(\omega,\beta)=\begin{cases}\dfrac{\left(1-|R_n|^2\right)^2}{\left|1-R_n^2e^{-2ik_{z0}d}\right|^2}, & \beta\le k_0\\ \dfrac{4[\mathrm{Im}(R_n)]^2e^{-2|k_{z0}|d}}{\left|1-R_n^2e^{-2ik_{z0}d}\right|^2}, & \beta>k_0\end{cases} \tag{5}$$

where the subscript $n=$ s, p, i.e., the s- or p-polarization;k_{z0} is the out-of-plane wavevector in the gap given by $k_{z0}=(k_0^2-\beta^2)^{1/2}$; d is the gap distance; $k_0=\omega/c$is the vacuum wavevector; and R_n is the total Fresnel reflection coefficient of each structure unit, as seen in Fig. 1b) for example. For suspended thin layers under$\beta\le k_0$,$1-|R_n|^2$should be replaced by$1-|R_n|^2-|t_n|^2$, where t_n is the transmission coefficient [43].

For the system illustrated in Fig. 1a), the reflection coefficient R_n can be derived from the Fresnel equations for a four-layer structure shown in Fig. 1b) via the scattering matrix method [17,44]

$$R_n=\frac{r_n^{12}+R_n^2e^{2ik_z^nh_g}}{1-r_n^{12}R_n^2e^{2ik_z^nh_g}}, \tag{6}$$

$$R_n^2=\frac{r_n^{23}+r_n^{34}e^{2ik_z^nh_{\mathrm{hBN}}}}{1-r_n^{23}r_n^{34}e^{2ik_z^nh_{\mathrm{hBN}}}}, \tag{7}$$

where h_g and h_{hBN} are the thicknesses of the graphene and hBN layers, respectively; the subscript denotes the regions of the heterostructure as labeled in the inset in Fig. 1b, namely, 1, 2, 3, 4 corresponding to the air, graphene, hBN, and substrate layers. In consequence, r_n^{ij} is the reflectivity at the interface between layers i and j, decided by the Fresnel equations

$$r_s^{ij}=\frac{k_z^{is}-k_z^{js}}{k_z^{is}+k_z^{js}}, \tag{8}$$

$$r_p^{ij}=\frac{k_z^{ip}\varepsilon_\perp^i-k_z^{ip}\varepsilon_\perp^i}{k_z^{ip}\varepsilon_\perp^i+k_z^{ip}\varepsilon_\perp^i} \tag{9}$$

where

$$k_z^{is}=\left(\varepsilon_\perp^ik_0^2-\beta^2\right)^{1/2},\quad k_z^{ip}=\left(\varepsilon_\perp^ik_0^2-\frac{\varepsilon_\perp^i}{\varepsilon_\parallel^i}\beta^2\right)^{1/2}$$

To establish the connection between the NFRHT and surface polaritons between these bi-planar heterostructures, the dispersion relation for the cavity surface polariton modes supported by the vacuum gap can be calculated as the solution of the following equation [17].

$$1-R_n^2e^{-2ik_{z0}d}=0 \tag{10}$$

which is the denominator in the expression of ξ_p ($\beta>k_0$) in Eq. (5)).

For convenience, two dimensionless parameters are defined to quantitatively compare the NFRHT performances of various heterostructures. NFRHT enhancement factor θ is defined as the near-field heat flux transferred between these bi-planar heterostructures normalized by the far-field blackbody limit under the same thermal gradient, given by

$$\theta=q/\sigma_{\mathrm{SB}}\left(T_h^4-T_c^4\right), \tag{11}$$

where σ_{SB} is the Stefan-Boltzmann constant given as $\sigma_{\mathrm{SB}}=5.67\times10^{-8}\ W/(m^2K^4)$.

Meanwhile, relative NFRHT enhancement factor$\varphi$is defined to characterize the substrate effects by comparing NFRHT under cases of these heterostructures with and without substrates, calculated as

$$\varphi=\frac{q_{ws}-q_{wos}}{q_{wos}}, \tag{12}$$

where, the subscript "ws" and "wos" denote "with substrate" and "without substrate", respectively.

3. Results and discussions

In this section, the NFRHT behaviors of various bi-planar suspended structures are modeled and analyzed first as benchmarks. Then substrates including silica, SiC, and Au are respectively integrated and their effects on the NFRHT are examined, with the underlying mechanisms particularly addressed.

3.1. NFRHT properties in suspended structures

The NFRHT behaviors between bi-planar suspended structures, including graphene monolayers, hBN thin layers, and graphene/hBN heterostructures, have been well reported in previous literature [30–32]. Here, we reexamine them as benchmarks for better comparisons to stress the substrate effects.

As one can see in Fig. 2a) for the case of two graphene monolayers, the PTP maxima resemble the dispersion relation of the cavity SPP mode (Eq. (10)) that emerges from the hybridization of the SPP modes of the two vacuum-graphene interfaces. Notice that the PTP maxima lie to the right of the light line, indicating that these modes correspond to evanescent waves. Hence, it is strongly supported that the NFRHT originates from the contribution of the cavity surface polaritons in our systems. Besides, it is clear from Fig. 2 that the graphene/hBN heterostructure outperforms both the bi-planar graphene monolayers and hBN layers in terms of enhancing the NFRHT. This stems from the effective hybridization of SPPs in graphene and HPPs in hBN that forms into two new collective modes as hyperbolic plasmon–phonon polaritons (HPPPs) inside the two RBs and the surface plasmon-phonon polaritons (SPPPs) outside (Fig. 2c). It is worth noting that the distinction between the electrodynamics in HPPPs and SPPPs is evident [29]. The former features as guided waves that propagate through the entire

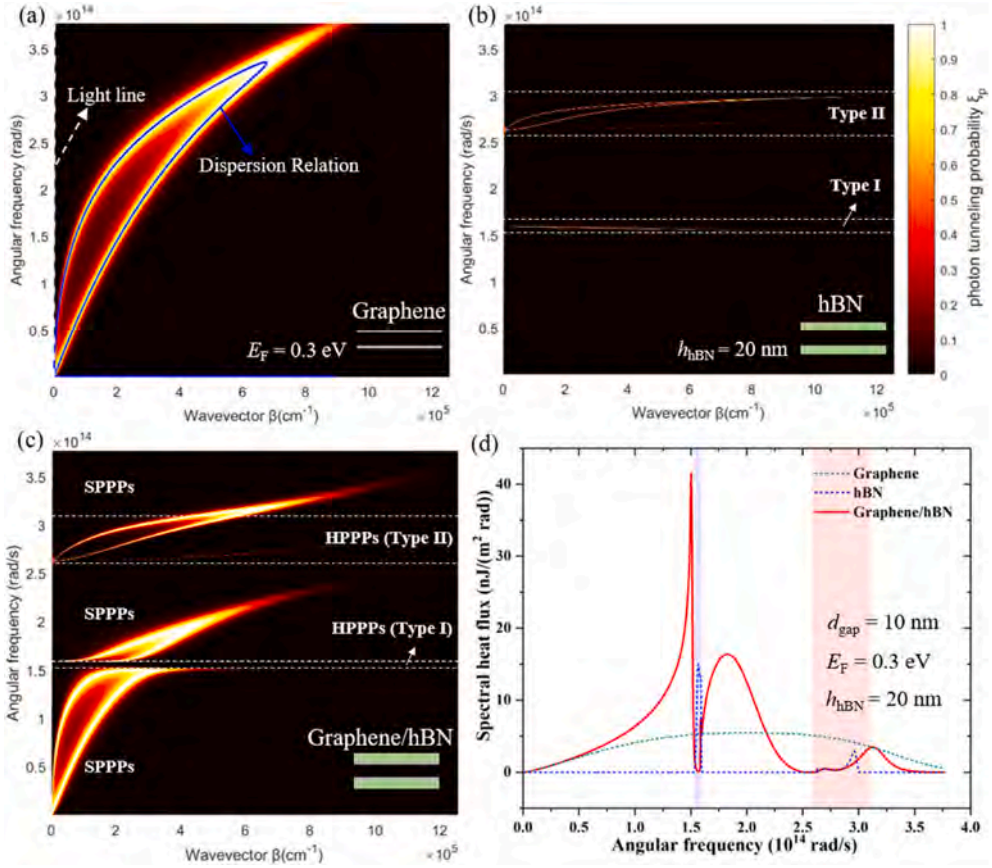

Fig. 2. NFRHT property for various suspended structures: contour maps of PTP for a) graphene monolayers; b) thin hBN layers; c) graphene/hBN heterostructures. d) Corresponding spectral heat flux distributions for the above three suspended structures. Note that the light line is plotted as the white dotted line and the dispersion relation of cavity SPPs between two graphene monolayers is plotted as the blue solid line in Fig.2 a). (For interpretation of the references to color in this figure legend, the reader is referred to the Web version of this article.)

graphene/hBN; while the latter is surface modes confined at the interface of graphene/hBN, which decay evanescently both inside the hBN layer and the vacuum. It is the evanescent field of these SPPPs decaying exponentially inside the vacuum gap that dominates the NFRHT. As displayed in Fig. 2c, the bright bands appear mainly within the frequency ranges outside the two hyperbolic bands, indicating highly efficient photon tunneling mediated via SPPPs. This phenomenon is also clearly illustrated by the two peaks of the spectral heat flux profile for the graphene/hBN heterostructures in Fig. 2d. Note that each bright band in the PTP contour maps (Fig. 2a–c) consists of two branches since these polaritonic modes are simultaneously excited on both surfaces of the emitter and receiver, which are also referred to as cavity modes [14, 25]. In addition, the general distinctions of characteristics in spectral distributions between SPPs and HPPs can also be observed in Fig. 2d. The SPP-mediated spectral heat flux for graphene monolayers with Fermi energy of 0.3 eV is quite broadband with frequencies ranging from 0 to 3.75 × 10^{14}rad/s but in a lower peak of about 5 nJ/(m^2 rad); while for 20-nm-thick hBN layers, HPPs are excited only within the two RB bands that result in the two sharp peaks of spectral heat flux profiles with a maximal peak value of about 15 nJ/(m^2 rad).

3.2. Substrates effects: enhancing or suppressing NFRHT?

In this section, the NFRHT between bi-planar graphene/hBN heterostructures is investigated by integrating them with various substrates including Au, SiC, and silica, respectively. Here these substrates were chosen because they are among the most commonly adopted substrates in plasmonics. Besides, silica and SiC are typical polar dielectric materials that support SPhPs within infrared ranges and enable significantly enhanced NFRHT; while metals as Au support SPPs within a wide range from visible to infrared, which hold great potential as thermal emitters due to their high carrier concentrations [45]. The effects of other substrates can be investigated using the same approach.

To study the substrate effects on the NFRHT, we start with cases where the hBN layer has a thickness of 1 nm, and the graphene Fermi energy is 0.3 eV which is easily accessible in experiments. The enhancement factor profiles in Fig. 3a indicate that the NFRHT between all these heterostructures is greatly enhanced by three to more than four orders of magnitude over the far-field blackbody radiation limit, due to the contribution of evanescent waves. It is also clear that each substrate exerts distinct impacts. The bi-planar heterostructures integrated with silica substrates outperform the other three configurations in terms of enhancing the NFRHT (Fig. 3a,c), especially at smaller gap spacing (below 50 nm). At $d = 10$ nm, the radiative heat flux between graphene/hBN/silica heterostructures (2087.93 kW/m^2) is 3.11-fold higher than that between the bare silica substrates (507.49 kW/m^2) and yields a further increase of 41.75% compared to that between the suspended graphene/hBN structures (1472.95 kW/m^2). This shows the huge potential for the 2D vdW material-based heterostructures to enhance NFRHT compared to the bulk materials as well as the possibility of substrate-assisted enhancement effect.

On the other side, at $d = 10$ nm, the integrations of both the Au and SiC substrates greatly suppress the NFRHT enhancement, reducing by a factor about 37% and 87%, respectively, compared to that of the suspended heterostructures. These effects can be more easily observed by the profiles of relative enhancement factor φ (Eq. (12)) in Fig. 3b. It is quite interesting to notice that these φ profiles keep almost flat under gap spacing smaller than 200 nm, indicating that these pronounced substrate effects remain nearly unchanged in this range. As the gap spacing continues increasing (>200 nm), the substrate effects either enhancing or suppressing NRFHT gradually weaken and tend to vanish in the far-field regime (Fig. 3b).

These substrate effects highly depend on the thickness of the middle hBN layer. As illustrated in Fig. 3c-d, although profiles of θ for all the

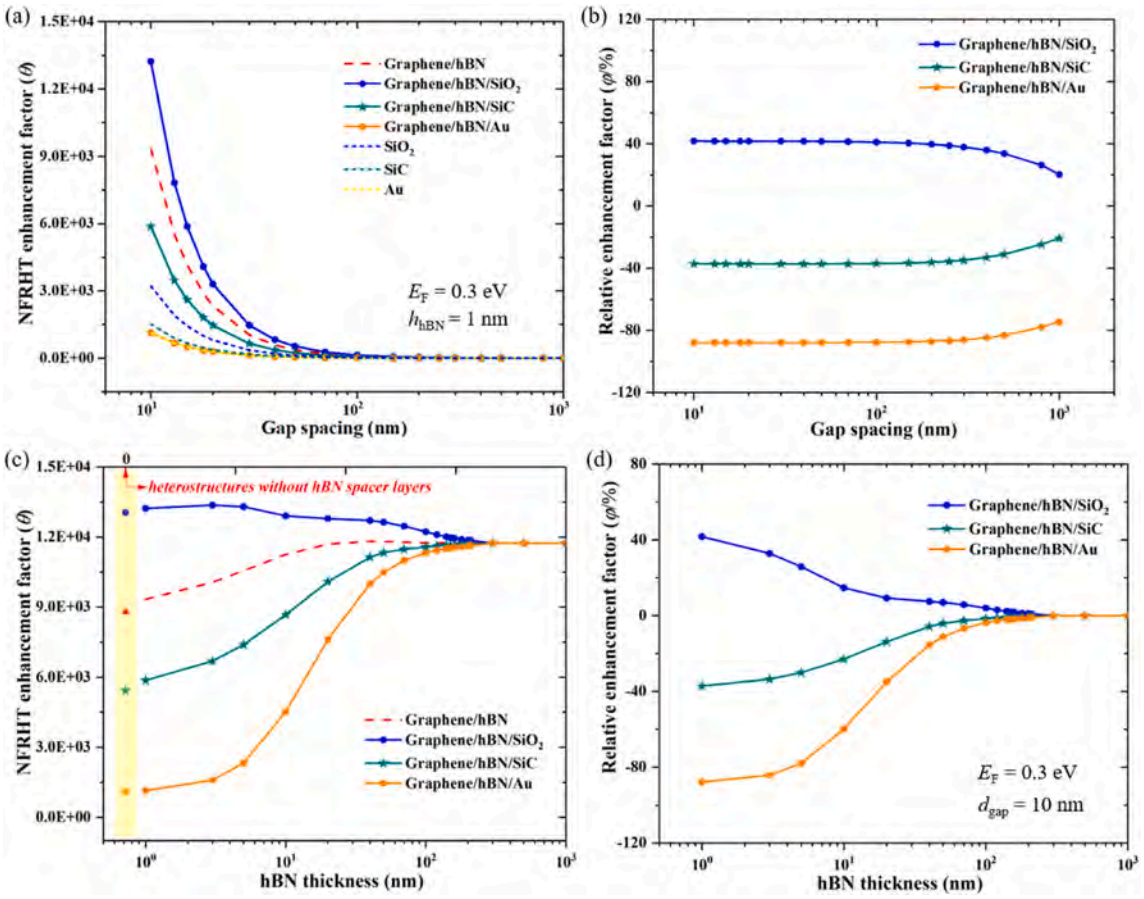

Fig. 3. Substrate effects on the NFRHT between various bi-planar heterostructures: a) NFRHT enhancement factor θ and b) relative enhancement factor φ as a function of gap spacing, at $h_{hBN} = 1$ nm and $E_F = 0.3$ eV; c) NFRHT enhancement factor θ and d) relative enhancement factor φ as a function of hBN thickness, at $E_F = 0.3$ eV and $d_{gap} = 10$ nm. Note that the markers in the yellow rectangle of Fig.3c denote the NFRHT enhancement factor for corresponding heterostructures without the middle hBN layer. (For interpretation of the references to color in this figure legend, the reader is referred to the Web version of this article.)

studied heterostructures evolve differently as the hBN thickness increases, they converge to a common constant as the hBN thickness is over 200 nm. These trends indicate the gradually weakened and finally negligible substrate effects with thicker hBN layers. This can be attributed to the thickness-dependent properties of surface polaritons and their coupling with various dielectric environments, where underlying mechanisms will be discussed in detail later. In addition, the NFRHT between those heterostructures without the middle hBN layer is also investigated, which is displayed in Fig. 3c as corresponding markers in the bright yellow rectangle. It shows that even the addition of a 1 nm-thick hBN film can contribute to enhancing the NFRHT between all these heterostructures, both those suspended and substrate-integrated ones, thanks to the effective hybridization of SPPs in graphene and HPPs in hBN. This in turn implies the great potential of hBN to further enhance the NFRHT of graphene-based heterostructures.

3.3. Underlying mechanisms

To elucidate the underlying mechanisms of these substrate effects, the PTP contour maps are plotted and compared in Fig. 4a–i. The substrate can greatly modify the NFRHT since it provides the dielectric environment that interacts with the hybridized polaritons in the graphene/hBN heterostructures, through either further polaritonic couplings or causing extra energy losses. The former may further enhance the NFRHT but occurs only within frequencies that have overlapped ranges; while the latter dampens most of the polaritonic energy, thus leading to largely reduced NFRHT.

For graphene/hBN/silica heterostructures, the SPhPs in silica substrate further couple with SPPPs within its characteristic frequency ranges due to the wide resonant frequency overlap. Compared with the PTP contour maps of graphene/hBN in Fig. 2c, the bright bands mediated by SPPPs are distinctively altered due to the existence of silica phonons (Fig. 4a,d), indicating the strong coupling between SPPPs in graphene/hBN and the SPhPs in silica. This leads to the resonant enhancement of the hybridized modes that further boost the NFRHT, as clearly illustrated by the increased area enclosed by the spectral heat flux in this range (Fig. 4h). Note that the shapes of the bright bands mediated by SPhPs in silica are partially preserved in Fig. 4d, implying the contributions of silica phonons to the NFRHT. In contrast, the silica exerts limited impacts on the HPPPs in the two RB bands, and so is the resultant NFRHT in these two regions. Hence, the substrate-assisted enhancement effect is the direct result of the contributions from SPhPs in the silica substrate and its effective coupling with SPPPs in graphene/hBN.

For cases of the SiC substrate, similar coupling between SPPPs and SPhPs in SiC occurs within ranges of 1.52–1.8 $\times 10^{14}$rad/s, illustrated by the PTP contour map that preserves the feature of SPhPs in SiC (Fig. 4b,e). But it contributes little to the NFRHT enhancement due to this very narrow overlapped range, outside which the energy carried by SPPPs is considerably dampened (Fig. 4e,h). As a result, the SiC substrate largely suppresses the NFRHT enhancement. When it comes to the graphene/hBN/Au heterostructures, the Au substrate damps the most polaritonic energy carried by SPPPs, leading to the lowest NFRHT enhancement among all the configurations (Fig. 4f,h). This large damping effect can be indicated by the large imaginary part of the dielectric constant for Au, particularly in the IR regime (Fig. S1b). It is

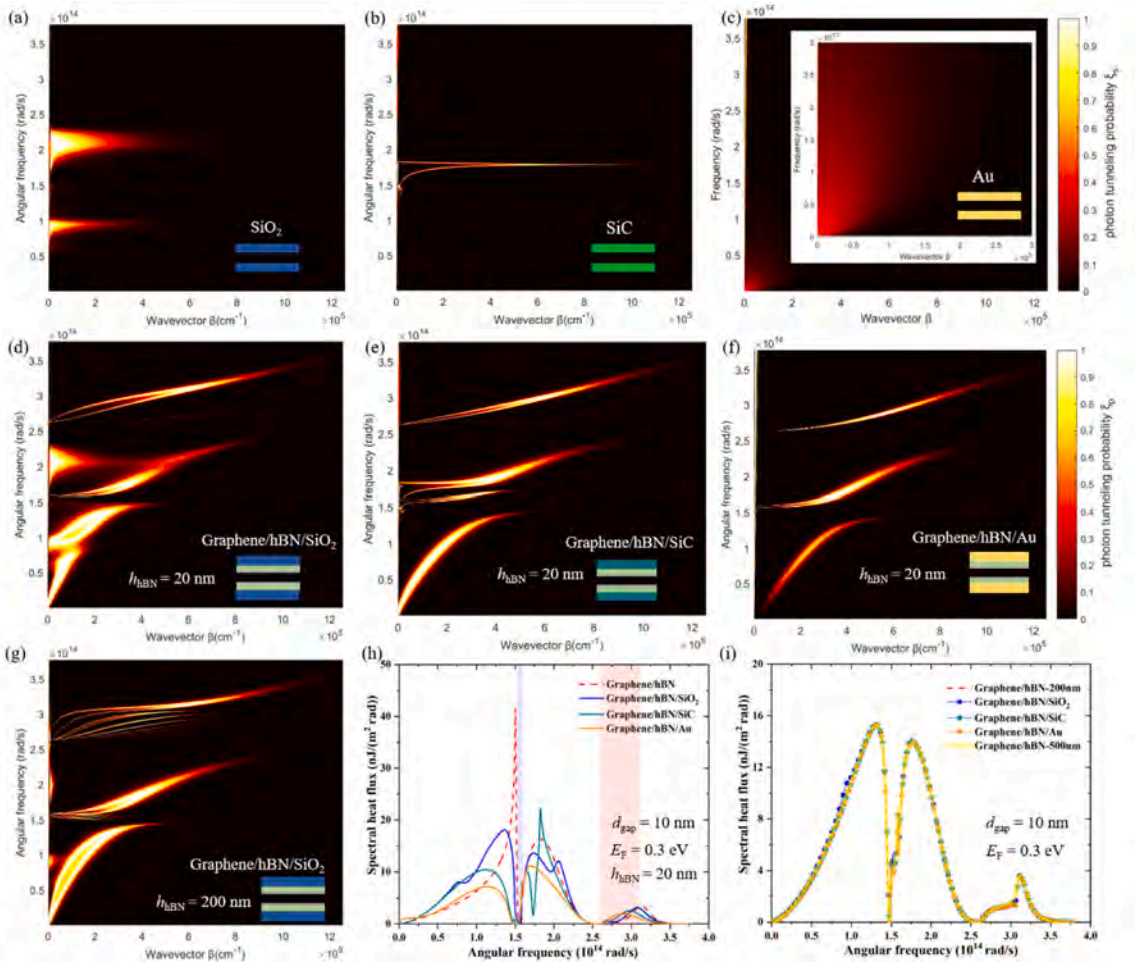

Fig. 4. Mechanisms for NFRHT enhancement of various bi-planar heterostructures. a-c) Contour maps of PTP for bared substrates: a) silica; b) SiC; c) Au; d-g) PTP contour maps for graphene/hBN heterostructures integrated with substrate d) silica; e) SiC; f) Au with $h_{hBN} = 20$ nm, and g) silica with $h_{hBN} = 200$ nm, at $E_F = 0.3$ eV, $d_{gap} = 10$ nm. Note that all PTP contour maps display the $\xi_p$and share the same colorbar as Fig.4f, except for Fig.4e which denotes ξ_s. h-i) Spectral heat flux between corresponding heterostructures with e) $h_{hBN} = 20$ nm and f) $h_{hBN} = 200$ nm, the yellow solid line denoting spectral heat flux of graphene/hBN heterostructure with $h_{hBN} = 500$ nm for better ξ_p comparison. (For interpretation of the references to color in this figure legend, the reader is referred to the Web version of this article.)

also noteworthy that the dominant contribution to the flux between Au substrates is due to eddy currents induced by the s-polarized magnetic field [46] (Fig. 4c), suggesting that no further coupling with SPPPs exists. In a word, the final substrate effect comes from the competition between the further enhancement mediated by the effective polaritonic coupling and the weakened effect induced by the dielectric losses to the original polaritonic energy. Substrate-assisted enhancement for the NFRHT can be achieved by properly selecting substrates that have not only wide overlapped resonant frequency ranges with the SPPPs in graphene/hBN but also low dielectric losses, just like the silica substrate.

As for the thickness-dependent NFRHT property, the main mechanism lies in the screening effect of the middle hBN layer rather than the thickness-dependent HPPs excited in hBN. Comparing the PTP contours in Fig. 4d and g, it is clear that higher orders of HPPPs appear at lower wavevector β in both hyperbolic bands in a thicker hBN layer. But this results in insignificant changes in spectral heat flux since the bright bands also vanish at lower wavevectors in this thicker layer. This trend can be more clearly observed in the PTP contour maps in the SI (Figs. S3a–f) for singe hBN layers with various thicknesses. Contrarily, SPPPs excited in graphene/hBN heterostructure are insensitive to the hBN thickness but very susceptible to the dielectric environment, since they are surface modes that propagate along the heterostructure interface and the substrate. More energy mediated by SPPPs tends to dissipate on the substrate with thinner hBN layers, thus resulting in less photonic energy being radiated and transferred through the vacuum gap. As the hBN thickness grows thicker, especially when the thickness is beyond the penetration depth of the evanescent field of SPPPs (about 200 nm in this case) [14], the carried polaritonic energy is well preserved with little loss and thus the NFRHT achieves its maximum for most heterostructures (Fig. 3c). Heterostructures integrated with the silica substrates are the exception since the NFRHT enhancement decreases with thicker hBN (<200 nm). The reason lies in that the contribution of the phonons in silica to enhancing NFRHT is also increasingly screened by the thicker hBN spacer layer. This phenomenon can be illustrated by the almost vanishing bright bands mediated by SPhPs of silica in Fig. 4g, together with the nearly overlapped profiles of spectral heat flux for various heterostructures with hBN thickness no less than 200 nm in Fig. 4i. Corresponding PTP contour maps are better compared in Fig. S4, where the distributions of bright bands for all the substrate-integrated heterostructures recover to that of the suspended graphene/hBN with 200-nm-thick-hBN. Here the penetration depth of the SPPPs in hBN is the length scale over which SPPPs can exert their influence on the electrodynamics of surrounding media [29], beyond which the phonons and other substrate effects are indiscriminately screened by the hBN layer. In this case, the substrate selection no longer makes difference to the NFRHT.

The polaritonic coupling in graphene/hBN strongly depends on the Fermi energy of graphene E_F, and so does the NFRHT between these bi-

planar heterostructures. Thus, a series of simulations were also conducted to investigate the substrate effects under various Fermi energies. It is quite interesting to find that each substrate effect on NFRHT, indeed, varies as the Fermi energy changes, but the underlying mechanisms can also be attributed to the competing between the dielectric losses and polaritonic couplings. The maximal heat flux can be achieved for each bi-planar heterostructure at an optimal Fermi energy where these two mechanisms were well compromised. One can find more detailed discussions in the SI.

4. Conclusion

This study theoretically investigated the effects of various substrates on the NFRHT between bi-planar graphene/hBN heterostructures, thus facilitating this kind of 2D layered heterostructures to go further into practice. The main finding is that under $E_F = 0.3$ eV, both the Au and SiC substrates suppress the NFRHT enhancement while the silica further improves it, compared to the suspended configurations. Besides, these substrate effects highly depend on the thickness of the middle hBN spacer layer with a critical length determined by the penetration depth of evanescent fields of related SPs. Within this critical length, the substrate exerts increasingly weakened impacts on the NFRHT with thicker hBN layers, due to the competition between the polaritonic coupling and the dielectric losses; otherwise, the hBN itself is thick enough to screen all these effects. In turn, this also shows the tunability of NFRHT between heterostructures by passively tailoring the thickness of hBN or the dielectric environment of substrates. These findings will be instructive to the experimental implementation and device integration of related NFRHT-based applications.

Declaration of competing interest

The authors declare that they have no known competing financial interests or personal relationships that could have appeared to influence the work reported in this paper.

Data availability

Data will be made available on request.

Acknowledgments

This work was supported by the National Natural Science Foundation of China (Grant No. 51925203) and the Strategic Priority Research Program of Chinese Academy of Sciences (Grant No. XDB36000000).

Appendix A. Supplementary data

Supplementary data to this article can be found online at https://doi.org/10.1016/j.ijthermalsci.2022.107493.

References

[1] G.R. Bhatt, B. Zhao, S. Roberts, I. Datta, A. Mohanty, T. Lin, J.M. Hartmann, R. St-Gelais, S. Fan, M. Lipson, Integrated near-field thermo-photovoltaics for heat recycling, Nat. Commun. 11 (2020) 1–7, https://doi.org/10.1038/s41467-020-16197-6.

[2] A. Fiorino, L. Zhu, D. Thompson, R. Mittapally, P. Reddy, E. Meyhofer, Nanogap near-field thermophotovoltaics, Nat. Nanotechnol. 13 (2018) 806–811, https://doi.org/10.1038/s41565-018-0172-5.

[3] B. Guha, C. Otey, C.B. Poitras, S. Fan, M. Lipson, Near-field radiative cooling of nanostructures, Nano Lett. 12 (2012) 4546–4550, https://doi.org/10.1021/nl301708e.

[4] D. Thompson, L. Zhu, E. Meyhofer, P. Reddy, Nanoscale radiative thermal switching via multi-body effects, Nat. Nanotechnol. 15 (2020) 99–104, https://doi.org/10.1038/s41565-019-0595-7.

[5] Y. Zhang, W. Zhu, F. Hui, M. Lanza, T. Borca-Tasciuc, M. Muñoz Rojo, A review on principles and applications of scanning thermal microscopy (SThM), Adv. Funct. Mater. 30 (2020), https://doi.org/10.1002/adfm.201900892.

[6] Y. De Wilde, F. Formanek, R. Carminati, B. Gralak, P.A. Lemoine, K. Joulain, J. P. Mulet, Y. Chen, J.J. Greffet, Thermal radiation scanning tunnelling microscopy, Nature 444 (2006) 740–743, https://doi.org/10.1038/nature05265.

[7] B.C. Stipe, T.C. Strand, C.C. Poon, H. Balamane, T.D. Boone, J.A. Katine, J.L. Li, V. Rawat, H. Nemoto, A. Hirotsune, O. Hellwig, R. Ruiz, E. Dobisz, D.S. Kercher, N. Robertson, T.R. Albrecht, B.D. Terris, Magnetic recording at 1.5Pbm-2 using an integrated plasmonic antenna, Nat. Photonics 4 (2010) 484–488, https://doi.org/10.1038/nphoton.2010.90.

[8] M. Fedoruk, M. Meixner, S. Carretero-Palacios, T. Lohmüller, J. Feldmann, Nanolithography by plasmonic heating and optical manipulation of gold nanoparticles, ACS Nano 7 (2013) 7648–7653, https://doi.org/10.1021/nn402124p.

[9] K. Kim, B. Song, V. Fernández-Hurtado, W. Lee, W. Jeong, L. Cui, D. Thompson, J. Feist, M.T.H. Reid, F.J. García-Vidal, J.C. Cuevas, E. Meyhofer, P. Reddy, Radiative heat transfer in the extreme near field, Nature 528 (2015) 387–391, https://doi.org/10.1038/nature16070.

[10] V. Chiloyan, J. Garg, K. Esfarjani, G. Chen, Transition from near-field thermal radiation to phonon heat conduction at sub-nanometre gaps, Nat. Commun. 6 (2015) 6755, https://doi.org/10.1038/ncomms7755.

[11] A. Principi, M.B. Lundeberg, N.C.H. Hesp, K.J. Tielrooij, F.H.L. Koppens, M. Polini, Super-planckian electron cooling in a van der Waals stack, Phys. Rev. Lett. 118 (2017) 1–6, https://doi.org/10.1103/PhysRevLett.118.126804.

[12] C. Lucchesi, R. Vaillon, P.-O. Chapuis, Radiative heat transfer at the nanoscale: experimental trends and challenges, Nanoscale Horizons 6 (2021) 201–208, https://doi.org/10.1039/D0NH00609B.

[13] C.R. Otey, L. Zhu, S. Sandhu, S. Fan, Fluctuational electrodynamics calculations of near-field heat transfer in non-planar geometries: a brief overview, J. Quant. Spectrosc. Radiat. Transf. 132 (2014) 3–11, https://doi.org/10.1016/j.jqsrt.2013.04.017.

[14] B. Song, D. Thompson, A. Fiorino, Y. Ganjeh, P. Reddy, E. Meyhofer, Radiative heat conductances between dielectric and metallic parallel plates with nanoscale gaps, Nat. Nanotechnol. 11 (2016) 509–514, https://doi.org/10.1038/nnano.2016.17.

[15] L. Wang, M. Bie, W. Cai, L. Ge, Z. Ji, Y. Jia, K. Gong, X. Zhang, J. Wang, J. Xu, Giant near-field radiative heat transfer between ultrathin metallic films, Opt Express 27 (2019) 36790, https://doi.org/10.1364/oe.27.036790.

[16] T. Králík, P. Hanzelka, V. Musilová, A. Srnka, P. Urban, Near field radiative heat transfer between macro-scale metallic surfaces at cryogenic temperatures, Cryogenics 113 (2021) 1–6, https://doi.org/10.1016/j.cryogenics.2020.103156.

[17] B. Song, Y. Ganjeh, S. Sadat, D. Thompson, A. Fiorino, V. Fernández-Hurtado, J. Feist, F.J. Garcia-Vidal, J.C. Cuevas, P. Reddy, E. Meyhofer, Enhancement of near-field radiative heat transfer using polar dielectric thin films, Nat. Nanotechnol. 10 (2015) 253–258, https://doi.org/10.1038/nnano.2015.6.

[18] R. St-Gelais, L. Zhu, S. Fan, M. Lipson, Near-field radiative heat transfer between parallel structures in the deep subwavelength regime, Nat. Nanotechnol. 11 (2016) 515–519, https://doi.org/10.1038/nnano.2016.20.

[19] S.V. Boriskina, J.K. Tong, Y. Huang, J. Zhou, V. Chiloyan, G. Chen, Enhancement and tunability of near-field radiative heat transfer mediated by surface plasmon polaritons in thin plasmonic films, Photonics 2 (2015) 659–683, https://doi.org/10.3390/photonics2020659.

[20] X.L. Liu, R.Z. Zhang, Z.M. Zhang, Near-field radiative heat transfer with doped-silicon nanostructured metamaterials, Int. J. Heat Mass Tran. 73 (2014) 389–398, https://doi.org/10.1016/j.ijheatmasstransfer.2014.02.021.

[21] X.L. Liu, R.Z. Zhang, Z.M. Zhang, Near-field thermal radiation between hyperbolic metamaterials: graphite and carbon nanotubes, Appl. Phys. Lett. 103 (2013), https://doi.org/10.1063/1.4832057.

[22] H. Iizuka, S. Fan, Significant enhancement of near-field electromagnetic heat transfer in a multilayer structure through multiple surface-states coupling, Phys. Rev. Lett. 120 (2018) 63901, https://doi.org/10.1103/PhysRevLett.120.063901.

[23] M. Lim, J. Song, S.S. Lee, B.J. Lee, Tailoring near-field thermal radiation between metallo-dielectric multilayers using coupled surface plasmon polaritons, Nat. Commun. 9 (2018) 1–9, https://doi.org/10.1038/s41467-018-06795-w.

[24] M. Luo, J. Zhao, M. Antezza, Near-field radiative heat transfer between twisted nanoparticle gratings, Appl. Phys. Lett. 117 (2020), https://doi.org/10.1063/5.0018329.

[25] V. Fernández-Hurtado, F.J. García-Vidal, S. Fan, J.C. Cuevas, Enhancing near-field radiative heat transfer with Si-based metasurfaces, Phys. Rev. Lett. 118 (2017) 1–6, https://doi.org/10.1103/PhysRevLett.118.203901.

[26] O. Ilic, M. Jablan, J.D. Joannopoulos, I. Celanovic, H. Buljan, M. Soljačić, Near-field thermal radiation transfer controlled by plasmons in graphene, Phys. Rev. B Condens. Matter 85 (2012) 1–4, https://doi.org/10.1103/PhysRevB.85.155422.

[27] Y. Zhang, H.L. Yi, H.P. Tan, Near-field radiative heat transfer between black phosphorus sheets via anisotropic surface plasmon polaritons, ACS Photonics 5 (2018) 3739–3747, https://doi.org/10.1021/acsphotonics.8b00776.

[28] L. Ge, Y. Cang, K. Gong, L. Zhou, D. Yu, Y. Luo, Control of near-field radiative heat transfer based on anisotropic 2D materials, AIP Adv. 8 (2018), https://doi.org/10.1063/1.5049471.

[29] S. Dai, Q. Ma, M.K. Liu, T. Andersen, Z. Fei, M.D. Goldflam, M. Wagner, K. Watanabe, T. Taniguchi, M. Thiemens, F. Keilmann, G.C.A.M. Janssen, S.E. Zhu, P. Jarillo-Herrero, M.M. Fogler, D.N. Basov, Graphene on hexagonal boron nitride as a tunable hyperbolic metamaterial, Nat. Nanotechnol. 10 (2015) 682–686, https://doi.org/10.1038/nnano.2015.131.

[30] K. Shi, F. Bao, S. He, Enhanced near-field thermal radiation based on multilayer graphene-hBN heterostructures, ACS Photonics 4 (2017) 971–978, https://doi.org/10.1021/acsphotonics.7b00037.

[31] B. Zhao, B. Guizal, Z.M. Zhang, S. Fan, M. Antezza, Near-field heat transfer between graphene/hBN multilayers, Phys. Rev. B 95 (2017) 1–9, https://doi.org/10.1103/PhysRevB.95.245437.
[32] B. Zhao, Z.M. Zhang, Enhanced photon tunneling by surface plasmon-phonon polaritons in graphene/hBN heterostructures, J. Heat Tran. 139 (2017) 1–8, https://doi.org/10.1115/1.4034793.
[33] V.W. Brar, M.S. Jang, M. Sherrott, S. Kim, J.J. Lopez, L.B. Kim, M. Choi, H. Atwater, Hybrid surface-phonon-plasmon polariton modes in graphene/monolayer h-BN heterostructures, Nano Lett. 14 (2014) 3876–3880, https://doi.org/10.1021/nl501096s.
[34] A. Vakil, N. Engheta, Transformation optics using graphene, Science 80 (332) (2011) 1291–1294, https://doi.org/10.1126/science.1202691.
[35] X.-T. Kong, X. Yang, Z. Li, Q. Dai, X. Qiu, Plasmonic extinction of gated graphene nanoribbon array analyzed by a scaled uniform Fermi level, Opt. Lett. 39 (2014) 1345, https://doi.org/10.1364/ol.39.001345.
[36] X. Guo, H. Hu, X. Zhu, X. Yang, Q. Dai, Higher order Fano graphene metamaterials for nanoscale optical sensing, Nanoscale 9 (2017) 14998–15004, https://doi.org/10.1039/c7nr05919a.
[37] H. Hu, X. Guo, D. Hu, Z. Sun, X. Yang, Q. Dai, Flexible and electrically tunable plasmons in graphene-mica heterostructures, Adv. Sci. 5 (2018) 1800175, https://doi.org/10.1002/advs.201800175.
[38] P. Li, I. Dolado, F.J. Alfaro-Mozaz, F. Casanova, L.E. Hueso, S. Liu, J.H. Edgar, A. Y. Nikitin, S. Vélez, R. Hillenbrand, Infrared hyperbolic metasurface based on nanostructured van der Waals materials, Science 80 (359) (2018) 892–896, https://doi.org/10.1126/science.aaq1704.
[39] Z. Yuan, R. Chen, P. Li, A.Y. Nikitin, R. Hillenbrand, X. Zhang, Extremely confined acoustic phonon polaritons in monolayer-hBN/metal heterostructures for strong light-matter interactions, ACS Photonics 7 (2020) 2610–2617, https://doi.org/10.1021/acsphotonics.0c00981.
[40] A. Woessner, M.B. Lundeberg, Y. Gao, A. Principi, P. Alonso-González, M. Carrega, K. Watanabe, T. Taniguchi, G. Vignale, M. Polini, J. Hone, R. Hillenbrand, F.H. L. Koppens, Highly confined low-loss plasmons in graphene-boron nitride heterostructures, Nat. Mater. 14 (2015) 421–425, https://doi.org/10.1038/nmat4169.
[41] D. Edward, Palik, Handbook of Optical Constants of Solids, Academic P, San Diego, USA, 1998.
[42] C.J. Fu, Z.M. Zhang, Nanoscale radiation heat transfer for silicon at different doping levels, Int. J. Heat Mass Tran. 49 (2006) 1703–1718, https://doi.org/10.1016/j.ijheatmasstransfer.2005.09.037.
[43] Q. Li, H. He, Q. Chen, B. Song, Thin-film radiative thermal diode with large rectification, Phys. Rev. Appl. 16 (2021) 1, https://doi.org/10.1103/PhysRevApplied.16.014069.
[44] S. Dai, Z. Fei, Q. Ma, A.S. Rodin, M. Wagner, A.S. McLeod, M.K. Liu, W. Gannett, W. Regan, K. Watanabe, T. Taniguchi, M. Thiemens, G. Dominguez, A.H. Castro Neto, A. Zettl, F. Keilmann, P. Jarillo-Herrero, M.M. Fogler, D.N. Basov, Tunable phonon polaritons in atomically thin van der Waals crystals of boron nitride, Science 80 (343) (2014) 1125–1129, https://doi.org/10.1126/science.1246833.
[45] Z. Wang, T.S. Luk, Y. Tan, D. Ji, M. Zhou, Q. Gan, Z. Yu, Tunneling-enabled spectrally selective thermal emitter based on flat metallic films, Appl. Phys. Lett. 106 (2015) 101104, https://doi.org/10.1063/1.4914886.
[46] P.O. Chapuis, S. Volz, C. Henkel, K. Joulain, J.J. Greffet, Effects of spatial dispersion in near-field radiative heat transfer between two parallel metallic surfaces, Phys. Rev. B Condens. Matter 77 (2008) 1–9, https://doi.org/10.1103/PhysRevB.77.035431.